



Contents lists available at ScienceDirect

## Journal of Non-Crystalline Solids

journal homepage: [www.elsevier.com/locate/jnoncrysol](http://www.elsevier.com/locate/jnoncrysol)

# Novel predictive methodology of amorphisation of gas-atomised Fe-Si-B alloy powders

Kenny L. Alvarez<sup>a,\*</sup>, Hasan Ahmadian Baghbaderani<sup>b,c</sup>, José M. Martín<sup>a</sup>, Nerea Burgos<sup>a</sup>, Paul McCloskey<sup>b</sup>, Julián González<sup>d</sup>, Ansar Masood<sup>b</sup>

<sup>a</sup> CEIT-Basque Research and Technology Alliance (BRTA), Paseo de Manuel Lardizabal 15, 20018, Donostia San Sebastián, Spain

<sup>b</sup> Tyndall National Institute, University College Cork, Lee Maltings, Dyke Parade, T12 R5CP, Cork, Ireland

<sup>c</sup> School of Physics and CRANN, Trinity College, D02 PN40, Dublin 2, Ireland

<sup>d</sup> Dept. of Materials Physics, University of the Basque Country, P<sup>o</sup> de Manuel Lardizabal 3, 20018, Donostia San Sebastián, Spain

## ARTICLE INFO

## Keywords:

Amorphous materials  
Amorphous forming ability  
Gas-atomization  
CALPHAD  
Metallic glasses  
Alloy design

## ABSTRACT

The present work is focused on developing amorphisation capability criteria to predict regions with high amorphous forming ability (AFA) in the Fe-Si-B phase diagram. First, the AFA of Fe-Si-B alloy powders was evaluated by conventional empirical glass forming parameters, which eventually did not guide to the best AFA alloy. Then, AFA analysis was extended to the ternary phase diagram, calculated using CALPHAD, along with superimposed mathematical model based on topological instability factor ( $\lambda$ ), estimated critical cooling rate ( $R_c$ ) and critical particle size ( $d_c$ ), to confine the phase diagram regions with larger AFA. The alloy with the highest AFA shows optimum atomic size mismatch when  $\lambda = 0.204$ . Furthermore, the optimal region in the phase diagram to design alloys with high AFA is where Fe<sub>2</sub>B is the first solid phase under equilibrium solidification. Within these two limits, the alloys with lower liquidus temperatures show the highest AFA for the gas-atomised powders.

## 1. Introduction

Since the discovery of disordered alloys by Duwez *et al.* [1] in the 1960s, amorphous metals have been extensively investigated for fundamental as well as technological applications, including structural, biomedical, aerospace, and energy conversion [2]. Amorphous metals are metastable materials, conventionally solidified in  $\sim 20 - 30 \mu\text{m}$  thick ribbons at ultra-high cooling rates ( $\sim 10^6 \text{ K/s}$ ) to maintain short-range order atomic structure. If the short-range atomic order of amorphous alloys is similar to the precursor melt and concurrently reveals a distinct glass transition temperature ( $T_g$ ) well below the crystallisation temperature ( $T_X$ ), the alloys are known as “metallic glasses (MGs)” [3,4]. Contrary to amorphous metals, MGs can sometimes be solidified at phenomenally low cooling rates (as low as natural cooling) [5,6]. The functionality of MGs can be remarkably augmented if the glass forming ability (GFA) (*i.e.*, ease of glass formation, which determines the critical cooling rate) is substantially increased. Glass formation involves the thermal stability of the liquid phase and the suppression of crystallisation kinetics upon the cooling of melts [7]. To synthesise MGs at

modest cooling rates, the kinetics of phase transformation and the mechanism of glass formation has emerged as an intriguing subject [8]. Why only specific alloys retain significant amorphisation capability, while others show a high degree of crystallisation during solidification, remains an open question to the material science community [8,9].

A large number of empirical glass forming parameters have been proposed to predict the GFA of alloys, though the origin of the majority criteria relies on the classical nucleation and growth theory [7]. For example, Turnbull demonstrated that when the reduced glass transition temperature ( $T_{rg} = T_g/T_l$ , being  $T_l$  the liquidus temperature) is higher than  $2/3$ , the homogenous crystal nucleation rate decreases and, as a result, the crystallisation kinetics becomes more sluggish [10,11]. Similarly, Donald & Davies [12] proposed a simple way to estimate the GFA of alloys with two or more elements using the rule of mixture liquidus temperature ( $\Delta T^*$ ). Furthermore, Inoue formulated three empirical rules to predict the GFA, stating that: (i) the alloy must contain at least three elements, (ii) the constituents should include a significant atomic size difference ( $\geq 12\%$ ), and (iii) a negative heat of mixing among the major constituents is preferable [13,14]. Several other GFA

\* Corresponding author.

E-mail address: [kalvarez@ceit.es](mailto:kalvarez@ceit.es) (K.L. Alvarez).

<https://doi.org/10.1016/j.jnoncrysol.2021.121151>

Received 1 July 2021; Received in revised form 27 August 2021; Accepted 30 August 2021

Available online 4 September 2021

0022-3093/© 2021 The Authors.

Published by Elsevier B.V. This is an open access article under the CC BY-NC-ND license

(<http://creativecommons.org/licenses/by-nc-nd/4.0/>).

**Table 1**  
DSC results of the as-atomised and sieved powders<sup>a</sup>.

Alloy #	Composition (at. %)	$T_X$ (°C)	$\Delta H_C$ (J/g)	$\Delta H$ (J/g) (as-atomised powder)	AF (%)
1	Fe <sub>70</sub> Si <sub>15</sub> B <sub>15</sub>	557	161.0	132.0	82
2	Fe <sub>70</sub> Si <sub>18</sub> B <sub>12</sub>	547	166.0	91.0	55
3	Fe <sub>72.5</sub> Si <sub>12.5</sub> B <sub>15</sub>	547	170.0	170.0	100
4	Fe <sub>75</sub> Si <sub>5</sub> B <sub>20</sub>	530	178.8	95.5	54
5	Fe <sub>75</sub> Si <sub>7.5</sub> B <sub>17.5</sub>	542	178.0	113.0	63
6	Fe <sub>75</sub> Si <sub>10</sub> B <sub>15</sub>	553	179.0	146.0	82
7	Fe <sub>75</sub> Si <sub>12.5</sub> B <sub>12.5</sub>	547	164.0	134.0	82
8	Fe <sub>75</sub> Si <sub>15</sub> B <sub>10</sub>	528	184 <sup>b</sup>	49.4	27
9	Fe <sub>77.50</sub> Si <sub>7.5</sub> B <sub>15</sub>	525	173.0	111.0	64
10	Fe <sub>80</sub> Si <sub>5</sub> B <sub>15</sub>	489	—	70.6	<27
11	Fe <sub>80</sub> Si <sub>12</sub> B <sub>8</sub>	—	—	—	0

<sup>a</sup>  $T_X$ : crystallisation temperature;  $\Delta H_C$ : crystallisation enthalpy;  $\Delta H$ : area of exothermic peak of partially amorphous powders (as-atomised); AF: amorphous fraction calculated with Eq. (A.2) shown in Appendix A.

<sup>b</sup> Value obtained from Ref [49,50].

parameters have been proposed, including  $\Delta T_X$  [15],  $S$  [16],  $\gamma$  [17],  $\delta$  [18],  $\theta$  [19],  $\gamma_m$  [20],  $\omega$  [21] and new  $\beta$  [22]. All these parameters use  $T_g$  to estimate the GFA. Despite that all these parameters have been demonstrated to be sufficiently accurate to measure the GFA of alloys, the critical cooling rate,  $R_c$ , and critical diameter,  $D_{max}$ , are still the most

direct and quantifiable parameters. Since  $R_c$  and  $D_{max}$  are challenging to be measured, other criteria like  $P$  [23],  $\sigma$  [24],  $\lambda$  [25],  $\alpha$  ( $= T_X/T_i$ ) and  $\beta$  ( $= 1 + \alpha$ ) [26] have been developed, which can be applied even for conventional amorphous alloys where  $T_g$  is not obvious. However, none of these criteria is valid for a broad range of MGs. Conventionally, the design of amorphous metals is frequently based on empirical rules, that is, a trial-and-error approach, which is time-consuming and costly, hence designing alloys with a high amorphous forming ability (AFA) using thermodynamic modelling would be a step forward [27,28].

Among the broad range of amorphous metals, Fe-based alloys are of significant importance for their high demand in power conversion applications [29–31]. One of the most investigated systems is Fe-Si-B, thanks to its unique capability to retain exceptional soft magnetic properties, high corrosion resistance, and excellent mechanical properties [32]. Fe-Si-B alloys are generally melt-spun into amorphous ribbons of  $\sim 20 \mu\text{m}$  in thickness at ultra-high cooling rates ( $\sim 10^6 \text{ K/s}$ ) [33]. One of the fundamental drawbacks of melt-spun ribbons is their shape; the very thin thickness and long length limit the fabrication of devices with complex geometries. Contrary to that, amorphous powders provide the flexibility to make complex shapes and, after coating with an electrical insulator layer, are considered an excellent material for high-frequency technological applications [34–36]. Amorphous powders are usually produced by gas-atomisation, which is a well-industrialised mass production technique to produce micron size powders. This process consists

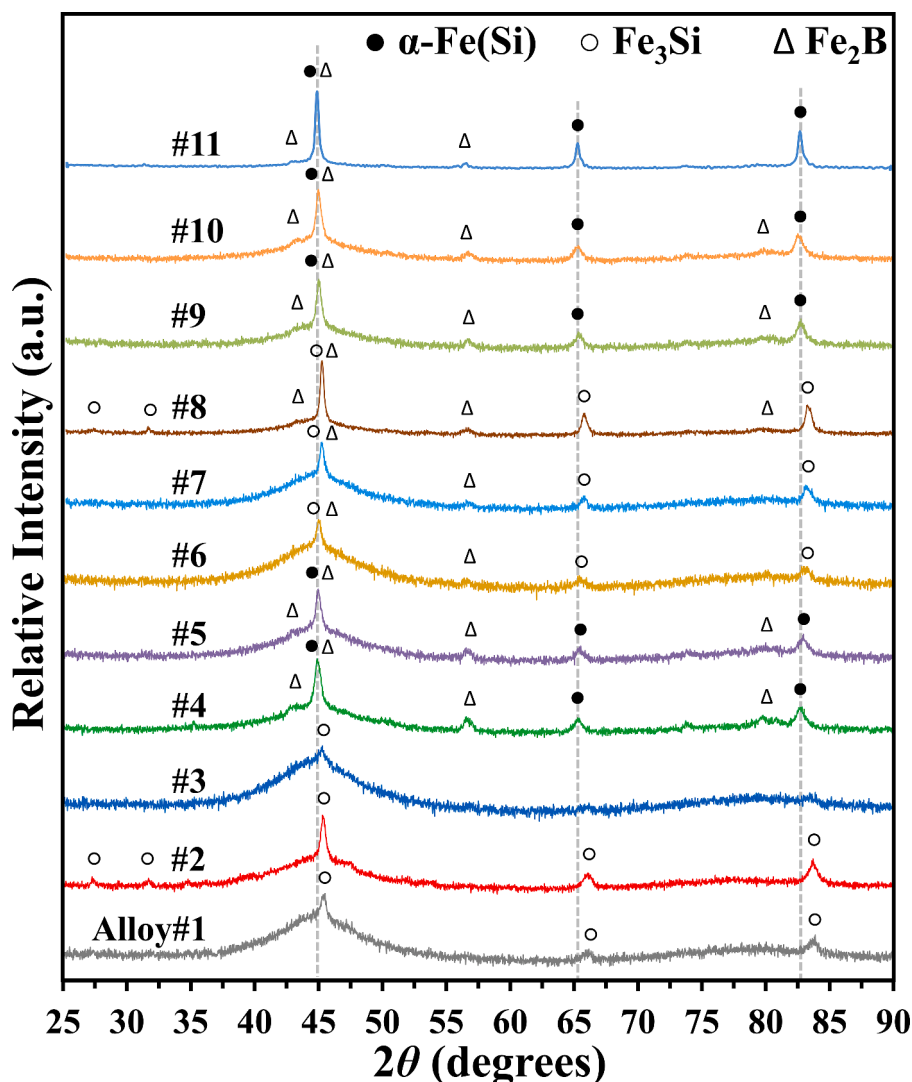


**Fig. 1.** XRD patterns of the as-atomised powders of alloys #1 to #11. Dashed grey lines correspond to the peaks positions of the phase  $\alpha$ -Fe(Si).

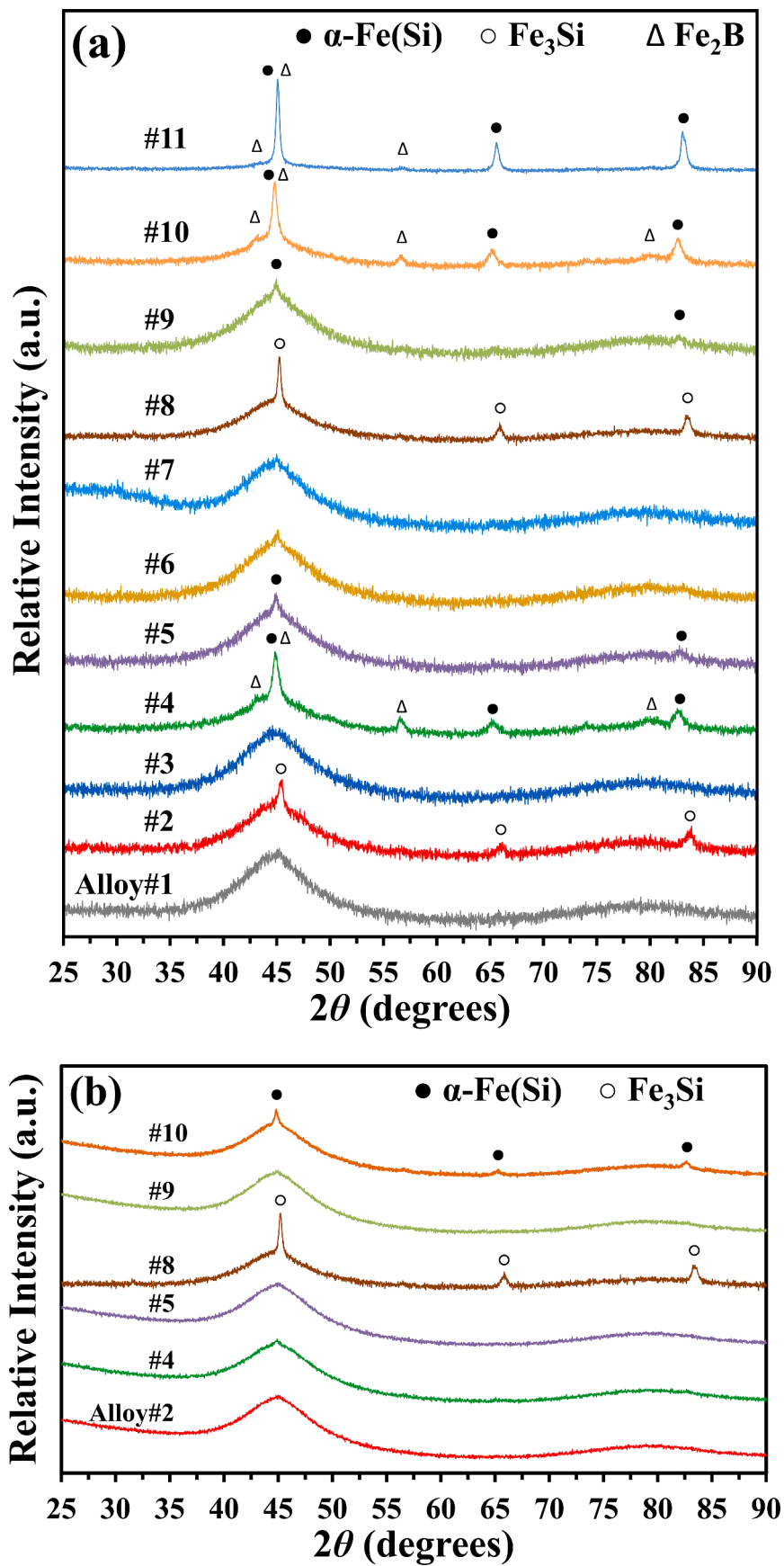


Fig. 2. a) XRD patterns of the sieved powders ( $<20\ \mu\text{m}$ ) of alloys #1 to #11 and (b) XRD patterns of the sieved powders ( $<10\ \mu\text{m}$ ) of alloys #2, #4, #5 and #8 to #10.

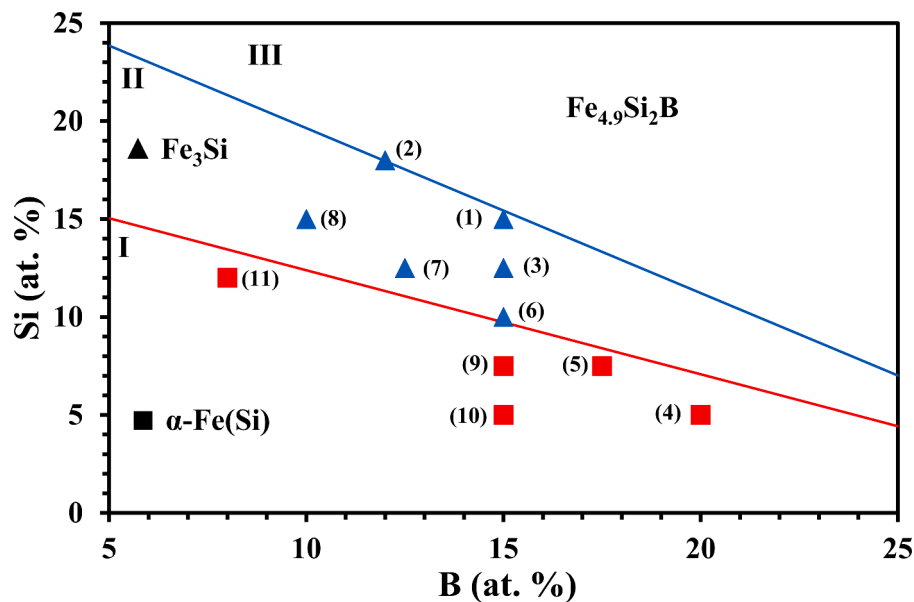


Fig. 3. Fe-rich corner of the ternary Fe-Si-B system showing the limits for the formation of the phases  $\alpha$ -Fe(Si) (■) and  $\text{Fe}_3\text{Si}$  (▲), according to the XRD results shown in Fig. 1 of the as-atomised alloys (alloys #1 to #11).

of breaking the liquid melt stream into droplets by using a supersonic gas flow. However, one of the fundamental limitations of gas-atomisation is the relatively low average cooling rate ( $\sim 10^4 - 10^5$  K/s) as compared to melt-spinning [37]. If the GFA of the alloys is not sufficiently high, the powders could exhibit a crystalline structure, deteriorating the soft magnetic performance and making them unsuitable for power conversion applications. Therefore, designing Fe-based alloys with high AFA that can be atomised as amorphous powders is essential to take advantage of the capabilities of these novel materials.

The present work is focused on establishing amorphisation capability criteria for Fe-Si-B powders by combining the CALPHAD (CALCulation of PHase Diagram) methodology with the topological instability factor ( $\lambda$ ). The new criteria were confirmed by selecting Fe-Si-B alloys within the high GFA region of the ternary phase diagram (Fe-rich). These alloys were gas-atomised into powders. Initially, the amorphisation capability of the alloys was evaluated using conventional empirical parameters, such as enthalpy of mixing,  $\Delta H^{\text{mix}}$ ,  $\alpha$ -, and  $\beta$ -parameters, but the trends predicted by these parameters were inconsistent with the experimental observations. Finally, the CALPHAD methodology was combined with  $\lambda$ -factor to obtain the highest amorphisation capability region inside the ternary Fe-Si-B system.

## 2. Materials and methods

The compositions of Fe-Si-B alloys were selected within the glass-forming region of the ternary phase diagram, as reported in the bibliography [38–40]. The gas atomisation experiments were carried out using a convergent-divergent, close-coupled atomiser in an atomisation unit PSI model Hermiga 75/3VI. Eleven different compositions of the ternary Fe-Si-B system were atomised (see compositions in Table 1). Regarding the raw materials, iron (supplied by Allied Metal Corp.), silicon (supplied by Cometal S.A.), and boron (supplied by H.C. Starck) of commercial purity were melted in an induction furnace. First, the chamber was purged with helium in order to evacuate the oxygen and avoid oxidation. Then, the temperature was increased by induction heating up to 1700 °C. The amount of powder produced per batch was nearly 2.5 kg. Helium at a pressure of 60 bar was used as atomising gas.

Thermal transitions were analysed by Differential Scanning Calorimetry (DSC). The powders were analysed using a TA Instrument DSC 2920. The experiments were performed using a sample of about 10 mg

on a copper pan with a lid, at a heating rate of 10 °C/min up to 700 °C and under an argon atmosphere. The crystallisation temperatures ( $T_x$ ), crystallisation enthalpies ( $\Delta H_C$ ), and energy released by partially amorphous powders (as-atomised,  $\Delta H$ ) were obtained from these experiments.

The structural characterisation of the powders was carried out via X-ray diffraction (XRD), using a diffractometer (Philips PW1825) and the characteristic wavelength of the  $K_\alpha$  line for Cu ( $\lambda = 1.542$  Å). The diffraction angle ( $2\theta$ ) varied from 25 ° to 90 ° at a scanning rate of 0.005 °/s, in steps of 0.02 ° with a holding time of 4 s at each diffraction angle. The particle size distribution of the powders was measured by laser diffraction in an instrument Sympatec Helos (H0852). The true density was measured in a He pycnometer Micrometrics Accupyc 1330.

Thermodynamic calculations and modelling have been carried out using PANDAT™ version 2019, using the thermodynamic database for multi-component Fe-rich alloys, PanIron. PANDAT™ is an integrated computational tool developed based on CALPHAD (CALCulation of PHase Diagram) approach for multi-component phase diagram calculations and materials properties simulations. The Fe-Si-B equilibrium phase diagram, including the liquidus temperatures ( $T_l$ ) and the solidified phases from the melt under equilibrium conditions were calculated using this software.

## 3. Results and discussion

### 3.1. Structural analysis of the powders

XRD patterns of the as-atomised powders, presented in Fig. 1, show the precipitation of different crystalline phases during the solidification process, which were identified as  $\alpha$ -Fe(Si),  $\text{Fe}_2\text{B}$ , and  $\text{Fe}_3\text{Si}$ . As can be seen in Fig. 1,  $\alpha$ -Fe(Si) and  $\text{Fe}_3\text{Si}$  have similar XRD patterns. However, there are two additional diffraction peaks at  $2\theta \approx 27$  and  $31$  ° corresponding to (111) and (200), which distinguish  $\text{Fe}_3\text{Si}$  [41] from  $\alpha$ -Fe(Si). In addition, as the lattice parameter of  $\text{Fe}_3\text{Si}$  [41] is twice that of  $\alpha$ -Fe(Si) [42],  $\text{Fe}_3\text{Si}$  shows diffraction peaks at slightly higher  $2\theta$ . A broad peak between  $2\theta = 35$  and  $55$  ° along with sharp Bragg's peaks indicate the simultaneous formation of amorphous and crystalline phases on gas-atomisation of alloys #1 to #10. Nevertheless, alloy #11 shows only sharp Bragg's peaks without a broad halo, demonstrating the full crystalline state of the powder. Interestingly, the relative area of the broad

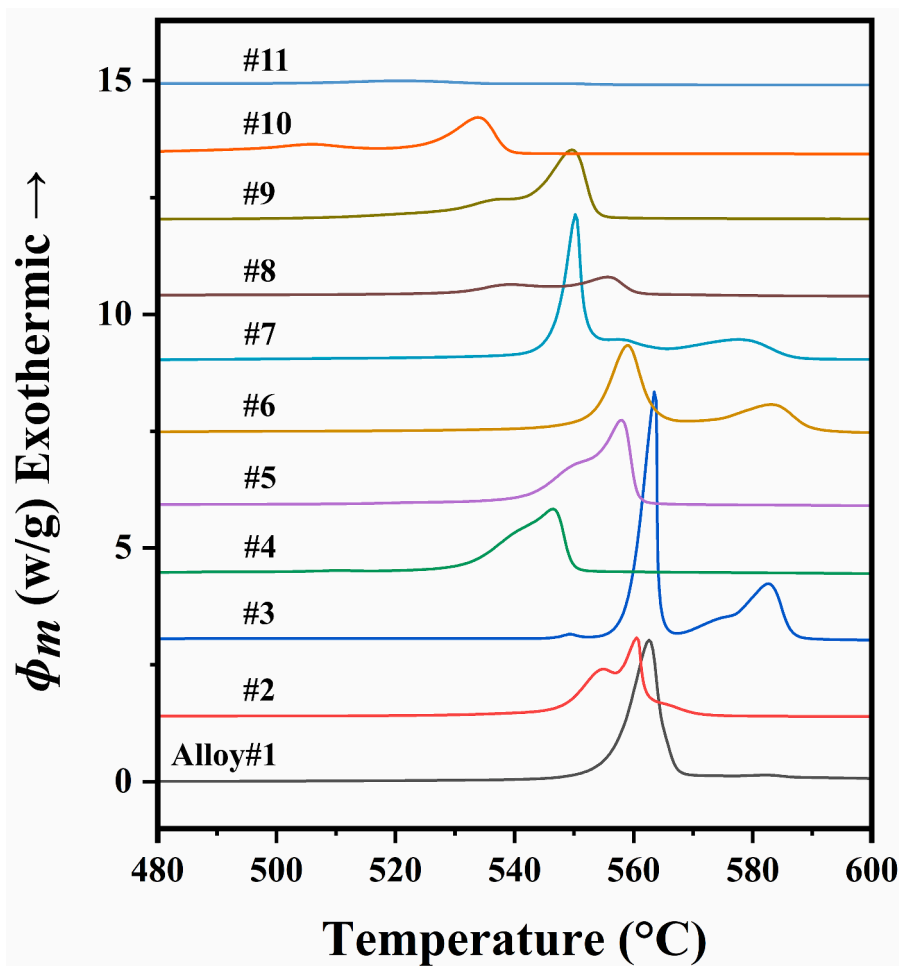


Fig. 4. DSC traces of the as-atomised powders of alloys #1 to #11.

halo and the broadening of the crystalline peaks is different in each alloy, indicating the varying weight fraction of amorphous and crystalline structures in each composition. For instance, alloy #3 shows a single broad peak at  $45^\circ$  ( $2\theta$ ) with a little shoulder kink, demonstrating the highest weight fraction of the amorphous phase in the investigated alloys. The small peak in alloy #3 is due to surface crystallisation in the largest particles (*i.e.*,  $>100\ \mu\text{m}$ ) due to the nature of the production process [43,44].

The cooling rate in gas atomisation is inversely proportional to the particle size (see Appendix A) [37], suggesting that the amorphisation is more likely in the smallest particle size fraction in each alloy. Accordingly, the as-atomised powders were sieved to separate the fraction  $<20\ \mu\text{m}$ . The XRD patterns of the sieved powders ( $<20\ \mu\text{m}$ ) of alloys #1, #3, #6 and #7 show only a broad halo between  $35$  and  $55^\circ$  ( $2\theta$ ) (Fig. 2(a)), confirming the amorphous nature of these alloys. Contrary to that, the other alloys (alloys #2, #4, #5, #8, #9, and #10) reveal Bragg's peaks of the crystalline phases, identified as  $\alpha\text{-Fe}(\text{Si})$ ,  $\text{Fe}_2\text{B}$ , and  $\text{Fe}_3\text{Si}$ . Interestingly, the relative intensity of the crystalline peaks in the sieved powders ( $<20\ \mu\text{m}$ ) was significantly smaller than in the as-atomised powders (see Fig. 1), confirming the higher weight fraction of amorphous phase in the fraction  $<20\ \mu\text{m}$  as compared to as-atomised powder. The higher amorphous fraction of sieved powders can be utilised as an "amorphisation capability indicator" for the alloys. On the other hand, the absence of the broad peak between  $35$  and  $55^\circ$  ( $2\theta$ ) in the fraction  $<20\ \mu\text{m}$  of alloy #11 confirms its fully crystalline structure.

Furthermore, in order to find the particle size below which fully amorphous structure can be found, the partially crystalline powders in the fraction  $<20\ \mu\text{m}$  (Fig. 2(a)) were further sieved to separate the

fraction  $<10\ \mu\text{m}$ . As can be seen in the XRD patterns shown in Fig. 2(b), the absence of Bragg's peaks in the fraction  $<10\ \mu\text{m}$  of alloys #2, #4, #5, and #9 confirms the amorphous nature of the particles below  $10\ \mu\text{m}$ . Conversely, alloys #8 and #10 exhibit crystalline structure even in the particles  $<10\ \mu\text{m}$ , which indicates the low amorphisation capability of these alloys.

Fig. 3 presents the nature of the crystalline phases formed as a function of Si and B content. The Fe-rich corner of the ternary Fe-Si-B system has been divided into three regions: below the dotted line (region-I), between dotted and dashed line (region-II) and above the dashed line (region-III). It is evident that the crystallisation of the  $\alpha\text{-Fe}(\text{Si})$  (B2) phase takes place in region-I, and the ordered  $\text{Fe}_3\text{Si}$  ( $\text{DO}_3$ ) phase crystallises in region-II, which agrees with a previous report [45]. Even if this work does not include any composition in region-III, it has been demonstrated that the phase  $\text{Fe}_{4.9}\text{Si}_2\text{B}$  precipitates when Si and B contents exceed 30 at.% [45,46]. Consequently, it can establish an upper and lower limit for the formation of  $\alpha\text{-Fe}(\text{Si})$  and  $\text{Fe}_3\text{Si}$  considering the amount of Si and B. In addition,  $\text{Fe}_2\text{B}$  phase precipitates in some as-atomised alloys (see Fig. 1), though no correlation between the  $\text{Fe}_2\text{B}$  and Si and B content can be established.

### 3.2. Amorphous fraction (AF) of as-atomised powders

The thermal transitions in the as-atomised powders were analysed using DSC presented in Fig. 4. The crystallisation starts in a broad temperature range, *i.e.*,  $T_X$  is comprised between  $489$  and  $553^\circ\text{C}$ , as summarised in Table 1. The powders reveal one, two, or three exothermic events, depending on the crystallisation mode of the alloys

**Table 2**  
Amorphisation capability parameters<sup>a</sup>.

Alloy #	Composition (at.%)	AF (%)	$\Delta H^{mix}$ (kJ/mol)	$A (= T_c/T_l)$	$B (= 1 + \alpha)$	$d_c$ ( $\mu\text{m}$ )	$R_c$ (K/s)	$T_l$ ( $^{\circ}\text{C}$ )	$\lambda$ -factor
1	Fe <sub>70</sub> Si <sub>15</sub> B <sub>15</sub>	82	-268800	0.469	1.469	43.6	3.0E+05	1188	0.220
2	Fe <sub>70</sub> Si <sub>18</sub> B <sub>12</sub>	55	-275856	0.480	1.480	16.7	2.1E+06	1139	0.214
3	Fe <sub>72.5</sub> Si <sub>12.5</sub> B <sub>15</sub>	100	-250475	0.452	1.452	96.1	6.3E+04	1210	0.204
4	Fe <sub>75</sub> Si <sub>5</sub> B <sub>20</sub>	54	-214100	0.411	1.411	21.5	1.2E+06	1290	0.197
5	Fe <sub>75</sub> Si <sub>7.5</sub> B <sub>17.5</sub>	63	-222600	0.431	1.431	30.9	6.0E+05	1257	0.193
6	Fe <sub>75</sub> Si <sub>10</sub> B <sub>15</sub>	82	-230400	0.453	1.453	43.3	3.1E+05	1220	0.188
7	Fe <sub>75</sub> Si <sub>12.5</sub> B <sub>12.5</sub>	82	-237500	0.465	1.465	55.4	1.9E+05	1177	0.183
8	Fe <sub>75</sub> Si <sub>15</sub> B <sub>10</sub>	27 <sup>b</sup>	-243900	0.447	1.447	8.8 <sup>b</sup>	7.6E+06 <sup>b</sup>	1180	0.179
9	Fe <sub>77.5</sub> Si <sub>7.5</sub> B <sub>15</sub>	64	-208575	0.431	1.431	31.8	5.8E+05	1217	0.172
10	Fe <sub>80</sub> Si <sub>5</sub> B <sub>15</sub>	<27	-185000	0.407	1.407	<10.0	>5.8E+06	1202	0.156
11	Fe <sub>80</sub> Si <sub>12</sub> B <sub>8</sub>	0	-206336	—	—	—	—	1261	0.143

<sup>a</sup> AF: amorphous fraction calculated with Eq. (A.2) shown in Appendix A;  $\Delta H^{mix}$ : enthalpy of mixing calculated by the procedure shown in Ref. [51];  $\alpha$  and  $\beta$ : GFA parameters [26];  $d_c$ : critical particle size calculated following the procedure shown in Appendix A;  $R_c$ : critical cooling rate estimated with Eq. (A.3) shown in Appendix A;  $T_l$ : liquidus temperature calculated by PANDAT<sup>TM</sup>;  $\lambda$ -factor: calculated by Eq. (1).

<sup>b</sup> Values calculated based on the crystallisation enthalpy obtained from amorphous wires from Ref [49,50] (see also Table 1).

(i.e., polymorphous, primary, or eutectic crystallisation [14]). Although alloy #1 exhibits only one crystallisation peak, the multi-crystallisation peak characteristic observed in alloys #2 to #10 can be attributed to the primary crystallisation mode [14,47]. Moreover, overlapped exothermic peaks in some alloys show that the crystallisation of the second and/or third phase starts even before the completion of the precipitation of the previous phase. The sharp peak characteristic observed in alloys #1, #3

and #7 indicates the compositional homogeneity of the crystallites precipitated during heating. Finally, it can be noted that the DSC trace of alloy #11 does not show any measurable crystallisation peak, confirming the fully crystalline microstructure of this alloy.

The heat released during crystallisation, i.e., the area under the crystallisation peaks, was used to calculate the amorphous fraction of the powders in the as-atomised state [48]. The crystallisation enthalpy

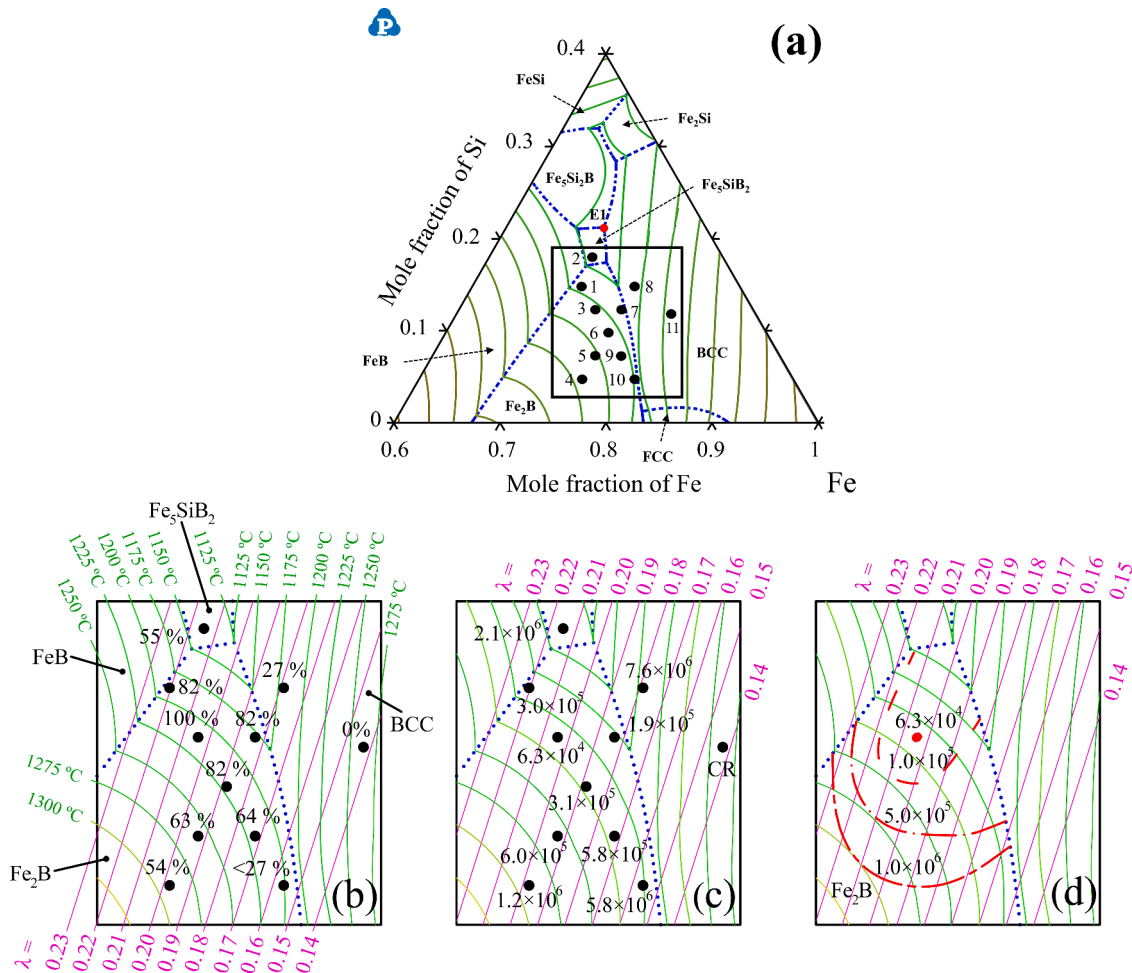


**Fig. 5.** a) Liquidus surface projection (blue dotted line) of the ternary Fe-Si-B diagram in the Fe-rich zone showing the investigated alloys (numbered black dots), eutectic point E1 (red dot), and the first equilibrium solid phase formed upon solidification; b) Amplified region showing  $\lambda$ -factor lines (solid magenta straight lines), AF (%) of all the investigated alloys and isotherms every 25  $^{\circ}\text{C}$  (green curved lines); c)  $R_c$  for all the investigated alloys; d) Estimated locus of constant  $R_c$  for  $1.0 \times 10^5$  K/s (red dashed line),  $5.0 \times 10^5$  K/s (red dash-dotted line) and  $1.0 \times 10^6$  K/s (red two-dashed line).

( $\Delta H_C$ ) of the amorphous phase of each alloy was obtained from the DSC trace of fully amorphous particles, separated by sieving and whose amorphous structure was confirmed by XRD (see Fig. 2). A partially amorphous structure results in the reduction of the energy released during crystallisation and, consequently, the area of the exothermic peaks is reduced. This area is proportional to the weight fraction (%) of the amorphous phase existing in the sample. The area of the exothermic peaks of partially amorphous as-atomised powders ( $\Delta H$ ) was divided by the crystallisation enthalpy ( $\Delta H_C$ ) to obtain the amorphous fractions (AF) in the as-atomised powders, as shown by Eq. (A.2) (see Appendix A). Since alloys #8 and #10 exhibited Bragg's peaks even in the fraction  $<10 \mu\text{m}$  (see Fig. 2(b)),  $\Delta H_C$  could not be measured for these compositions. The  $\Delta H_C$  of alloy #8 was obtained from the literature [49, 50], while for alloy #10,  $\Delta H_C$  was approximated by the area of the exothermic peak of partially amorphous particles of the fraction  $<10 \mu\text{m}$ ; consequently, AF of alloy #10 is not an exact value, but an upper boundary. The amorphous fraction (AF) in the as-atomised powders is summarised in Table 1. Alloy #3 reveals a 100% of amorphous fraction, which is in good agreement with XRD results (see Fig. 1). Furthermore, alloys #1, #6, and #7 revealed  $AF = 82\%$ , which is the second-highest AF among the investigated alloys. The AF of alloys #2, #4, #5, and #9 remained in the range of 54 to 64%. On the other hand, the AF of alloys #8 and #10 were estimated as 27% and  $<27\%$ , respectively, denoting the low amorphisation capability of these alloys. The AF of alloy #11 was found zero, since it did not show any measurable exothermic peak (see Fig. 4).

### 3.3. Evaluation of amorphisation capability of the alloys

The AF is a good indicator of the amorphisation capability of the alloys, and other parameters can be derived using AF, such as the critical particle size,  $d_C$ , and the critical cooling rate,  $R_C$  (see Appendix A for the calculation procedure). AF,  $d_C$ , and  $R_C$  can be used to gauge how useful conventional empirical criteria are to predict the amorphisation capability of gas-atomised powders. Different conventional amorphisation capability parameters of the investigated alloys were calculated and are summarised in Table 2. Since some of the alloys were amorphous and did not reveal any glass transition (or supercooled liquid region), only parameters that do not use  $T_g$  were analysed to estimate the AFA. Alloy #3 ( $\text{Fe}_{72.5}\text{Si}_{12.5}\text{B}_{15}$ ) has the highest amorphisation capability within the series of investigated alloys since it has the largest AF  $\sim 100\%$ , the largest  $d_C \sim 96 \mu\text{m}$ , and the lowest  $R_C \sim 6.3 \times 10^4 \text{ K/s}$ .

According to Inoue's empirical rules [13], the enthalpy of mixing,  $\Delta H^{\text{mix}}$ , significantly favours the formation of the amorphous structure and is a good indicator of the AFA. The more negative the  $\Delta H^{\text{mix}}$  is, the higher the AFA of an alloy. The enthalpy of mixing of the alloys is summarised in Table 2; the detailed calculation procedure is reported elsewhere [51]. Interestingly,  $\Delta H^{\text{mix}}$  does not correlate with the AF; the most negative  $\Delta H^{\text{mix}}$  was observed for alloy #2, which was partially amorphous ( $AF = 55\%$ ). In addition, the most negative  $\Delta H^{\text{mix}}$  coincides with the alloys showing the lowest  $T_l$  and, consequently, is the closest one to the deepest eutectic point (see Table 2). Similarly, no correlation was identified for  $\alpha$ - and  $\beta$ -parameters with the AF of the alloys [26], being the largest values of  $\alpha \sim 0.480$  and  $\beta \sim 1.480$  for the alloy #2, which has low AF = 55%, along with a small  $d_C \sim 16.7 \mu\text{m}$  and a high  $R_C \sim 2.1 \times 10^6 \text{ K/s}$ .

### 3.4. Establishing the amorphisation criteria for the alloys

The AFA was evaluated by combining thermodynamic modelling and the topological instability factor ( $\lambda$ ) of the Fe-Si-B alloys. The liquidus surface projection (blue dotted lines) of the Fe-Si-B phase diagram in the vicinity of the Fe-rich zone is presented in Fig. 5(a). Isothermal lines (solid green) are drawn to show how  $T_l$  decreases towards the eutectic point E1 (red dot). In addition, it displays the primary stable phases just below the liquidus temperature. The position of the Fe-Si-B alloys

investigated in the present study is indicated with numbered black spots.

The  $\lambda$ -factor of the Fe-Si-B alloys was calculated using Eq. (1), which only considers topological aspects and was initially proposed for binary alloys [25] and later extended to multi-component systems by Yan *et al.* [52]. This parameter describes the minimum solute concentration needed for producing material as amorphous and is defined as:

$$\lambda = \sum_{i=B}^Z C_i \cdot \left| \left( \frac{r_i}{r_A} \right)^3 - 1 \right| \quad (1)$$

where  $C_i$  is the solute atomic concentration (at. %),  $r_i$  is the solute atomic radius (nm), and  $r_A$  is the solvent atomic radius (nm). Assuming that the structure of amorphous metals can be modelled as an arrangement of icosahedral clusters, it has been proven that the optimal glass structure for numerous multi-component alloys is acquired when  $\lambda \simeq 0.18$  [52]. Recently, the use of  $\lambda$ -factor, along with CALPHAD methodology, was reported to predict the glass forming ability of ternary Zr-Fe-Al [53], Fe-Nb-B [54] and Co-Fe-B [55] bulk metallic glasses produced by Cu-mould casting and melt spinning, showing that the optimal value of  $\lambda$  can change from 0.14 to 0.22 depending on the composition. Consequently, in order to determine the optimal  $\lambda$ -factor for a given ternary system, this parameter should be validated experimentally.

Table 2 shows the  $\lambda$ -factor calculated for all the investigated alloys. The values range between 0.143 and 0.220. On the other hand, Fig. 5(b) to (d) display amplified the zone of Fig. 5(a) inside the black rectangle; in these enlarged figures,  $\lambda$ -factor lines and isothermal lines have been superimposed on the liquidus surface projection. The following information has been added in each one of these figures: i) AF (see Fig. 5(b)), ii)  $R_C$  (see Fig. 5(c)), and iii) locus of constant  $R_C$  for  $1.0 \times 10^5 \text{ K/s}$  (red dashed line),  $5.0 \times 10^5 \text{ K/s}$  (red dash-dotted line) and  $1.0 \times 10^6 \text{ K/s}$  (red two-dashed line) (see Fig. 5(d)).

The AFA of Fe-Si-B alloys has been analysed considering the information displayed in Fig. 5. The amorphisation criteria have been established as follow, depending on the first solid phase formed upon equilibrium solidification (*i.e.*, BCC,  $\text{Fe}_5\text{SiB}_2$  and  $\text{Fe}_2\text{B}$ ),  $T_l$  and  $\lambda$ -parameter:

- i) **BCC**: two alloys were atomised within this region, being one fully crystalline (alloy #11) and the other with  $AF = 27\%$  (alloy #8). Lowering the  $T_l$  plays a significant role in the amorphisation capability of alloys in this region; reducing  $T_l$  from  $1261 \text{ }^\circ\text{C}$  (alloy #11) to  $1180 \text{ }^\circ\text{C}$  (alloy #8) increased AF from 0 to  $\sim 27\%$  (see Table 2). Interestingly, it is possible to obtain melt-spun amorphous ribbons of compositions belonging to this region, as reported elsewhere [38–40]. The lower cooling rates in gas atomisation as compared to melt-spinning, however, do not allow producing a high fraction of amorphous phase in powders. The low AFA of alloy #11 could be attributed to the low  $\lambda = 0.143$ , compared to the optimal value (*i.e.*,  $\lambda = 0.18$ ), and the high  $T_l (= 1261 \text{ }^\circ\text{C})$ . On the other hand, alloy #8 with a good combination of  $\lambda = 0.179$  and low  $T_l = 1180 \text{ }^\circ\text{C}$  was expected to reveal high AF. Nevertheless, the low AF (= 27%) of alloy #8 suggests that the cooling rates in gas atomisation are not high enough to synthesise fully amorphous powders within this region. It seems that the region of the phase diagram where compositions are selected has a significant influence on the AFA. This can be easily pointed out by comparing alloy #8 with alloy #7; alloy #7 has similar  $\lambda$ -factor (= 0.183) and  $T_l (= 1177 \text{ }^\circ\text{C})$ , but AF of this alloy is 82%, *i.e.*, three times higher than in the case of alloy #8.
- ii)  **$\text{Fe}_5\text{SiB}_2$** : only one composition (alloy #2,  $\text{Fe}_{70}\text{Si}_{18}\text{B}_{12}$ ) was produced within this region, corresponding to the lowest  $T_l = 1139 \text{ }^\circ\text{C}$  (see Table 2). According to the bibliography, AFA significantly improves when  $T_l$  is lower or closer to the eutectic composition [14]. However, alloy #2 was only partially amorphous ( $AF = 55\%$ ), and  $R_C$  was as high as  $\sim 2.1 \times 10^6 \text{ K/s}$ , suggesting that a low  $T_l$  is not enough to produce the high AFA. The  $\lambda$ -factor of this alloy was calculated to be

0.214, which is significantly higher than the optimal value (*i.e.*,  $\lambda = 0.18$ ).

iii **Fe<sub>2</sub>B**: most of the compositions were produced within this region (8 samples), where *AF* varied from 54 to 100%. The results showed before suggest that this region is highly favourable for the formation of amorphous Fe-Si-B alloys. The best combination of *T<sub>l</sub>* and  $\lambda$ -factor was found for alloy #7 (*i.e.*, the lowest *T<sub>l</sub>* = 1177 °C in the region and  $\lambda = 0.183$  close to the optimal theoretical value). However, alloy #7 only retained an *AF* = 82%. Interestingly, alloy #3 revealed 100 % of amorphous structure, suggesting that the optimal experimental value of  $\lambda$ -factor for Fe-Si-B alloys is approximately 0.204. It seems that the *AF* of Fe-Si-B compositions systematically converges to 100% when they approach the composition of alloy #3 (see Fig. 5(b)). For instance, alloy #3 is encircled by alloys #1 ( $\lambda = 0.220$ ), #6 ( $\lambda = 0.188$ ) and #7 ( $\lambda = 0.183$ ), which revealed an *AF* = 82%. More interestingly, whereas alloys #9 (*T<sub>l</sub>* = 1217 °C) and #6 (*T<sub>l</sub>* = 1220) possess similar *T<sub>l</sub>* values and are in the same Fe<sub>2</sub>B region, *AF* rose from 64% in alloy #9 to 82% in alloy #6. This significant increase in *AF* can be attributed to the rise of  $\lambda$ -factor from 0.172 (alloy #9) to 0.188 (alloy #6), thus approaching the optimal experimental value of 0.204. This suggests that the  $\lambda$ -factor is one of the most critical parameters for the amorphisation capability criteria of the Fe-Si-B alloys.

These results can be used as an instrument to carefully select compositions of the ternary Fe-Si-B system with high AFA. For example, Fig. 5(c) can be used to select compositions whose critical cooling rate (*R<sub>c</sub>*) is just below the average cooling rate characteristic of the technique used to synthesize the alloy. Furthermore, the proposed methodology to establish the optimum AFA region, -combining CALPHAD, the topological instability factor ( $\lambda$ ), and gas atomisation for experimental validation- could be extended to other systems where the formation of amorphous phases is challenging.

#### 4. Conclusions

According to the presented results, alloys with high amorphisation capability in the Fe-Si-B system can be designed by using the following

#### Appendix A

The average cooling rate of non-crystalline alloy particles during gas atomisation ( $\left(\frac{\Delta T_d}{\Delta t}\right)$ ) can be estimated using the following simplified equation [56,57]:

$$\left|\frac{\Delta T_d}{\Delta t}\right| \approx \left|\frac{12}{\rho \cdot C_p} \cdot (T_d - T_f) \cdot \frac{k_g}{d^2}\right| \quad (\text{A.1})$$

where  $\rho$  is the density of the alloy,  $C_p$  the heat capacity,  $T_d$  the ambience temperature,  $T_f$  the furnace temperature,  $k_g$  the thermal conductivity of the atomising gas, and  $d$  the diameter of the particle.

Eq. (A.1) indicates that the cooling rate of a particle is inversely proportional to the square of its diameter, so small particles experience high cooling rates during gas atomisation, which consequently increases the fraction of the amorphous phase. Based on this fact, the fully amorphous particles were separated from as-atomised powders using sieves with different opening meshes in order to find a particle size below which the powder is completely amorphous according to its XRD pattern. Then, the energy released upon heating by fully amorphous particles (*i.e.*, the crystallisation enthalpy,  $\Delta H_C$ ) and by the as-atomised powder (*i.e.*,  $\Delta H$ ) were measured by DSC. Finally, the amorphous fraction (*AF*) was calculated using the following equation [46,48,58]:

$$AF = \frac{\Delta H}{\Delta H_C} \quad (\text{A.2})$$

The possibility of amorphisation is higher in the smallest particles, but in general it is not possible to affirm that every particle containing amorphous phase is fully amorphous [58]. Particles with a size near the critical diameter may possess a mixture of amorphous and crystalline structures. In the particular case of Fe-Si-B powders, the amount of crystallites in the particles with amorphous phase is minimal [44]; therefore, it can be neglected. Thus, the fraction of amorphous phase calculated from Eq. (A.2) can be considered equal to the fraction of amorphous particles. The critical diameter ( $d_C$ ) was obtained from the cumulative particle size distribution of the as-atomised powder, determined by laser diffraction, using the *AF* calculated with Eq. (A.2), as explained in reference [46]. The critical diameter values are reported in Table 2. The critical cooling rate (*R<sub>c</sub>*), also

rules:

- i Not all regions of the phase diagram are suitable to obtain amorphous alloys. For the Fe-Si-B system, the compositions in the region where Fe<sub>2</sub>B is the first solid phase formed upon equilibrium solidification have higher AFA as compared to others.
- ii The relative solute/solvent concentration should be such that  $\lambda$ -factor values vary in the range of 0.18 to 0.22. More specifically, the highest AFA is achieved when the  $\lambda$ -factor is approximately 0.204.
- iii Within limits fixed by the two previous criteria, the alloys with lower liquidus temperature (*i.e.*, closer to the eutectic composition) will have higher amorphisation capability.

Given a production method with a characteristic average cooling rate, these criteria can be used to design ternary Fe-Si-B alloys with a high enough AFA (*i.e.*, with a low enough critical cooling rate) to be obtained with an amorphous structure.

#### CRediT authorship contribution statement

**Kenny L. Alvarez**: Conceptualization, Methodology, Formal analysis, Investigation, Data curation, Writing – original draft, Visualization. **Hasan Ahmadian Baghbaderani**: Methodology, Formal analysis, Investigation, Data curation, Software, Writing – review & editing. **José M. Martín**: Conceptualization, Validation, Resources, Writing – review & editing, Supervision, Project administration, Funding acquisition. **Nerea Burgos**: Formal analysis, Investigation, Data curation, Software. **Paul McCloskey**: Resources, Writing – review & editing, Supervision, Project administration, Funding acquisition. **Julián González**: Conceptualization, Resources, Supervision. **Ansar Masood**: Conceptualization, Methodology, Validation, Investigation, Data curation, Writing – original draft.

#### Declaration of Competing Interest

The authors declare that they have no known competing financial interests or personal relationships that could have appeared to influence the work reported in this paper.

**Table A.1**Density ( $\rho$ ) of alloys #1 to 11.

Alloy #	Compositions (at.%)	$\rho$ (g/cm <sup>3</sup> )
1	Fe <sub>70</sub> Si <sub>15</sub> B <sub>15</sub>	6.89
2	Fe <sub>70</sub> Si <sub>18</sub> B <sub>12</sub>	6.84
3	Fe <sub>72.5</sub> Si <sub>12.5</sub> B <sub>15</sub>	6.96
4	Fe <sub>75</sub> Si <sub>5</sub> B <sub>20</sub>	7.20
5	Fe <sub>75</sub> Si <sub>7.5</sub> B <sub>17.5</sub>	7.07
6	Fe <sub>75</sub> Si <sub>10</sub> B <sub>15</sub>	7.05
7	Fe <sub>75</sub> Si <sub>12.5</sub> B <sub>12.5</sub>	7.02
8	Fe <sub>75</sub> Si <sub>15</sub> B <sub>10</sub>	7.04
9	Fe <sub>77.50</sub> Si <sub>7.5</sub> B <sub>15</sub>	7.13
10	Fe <sub>80</sub> Si <sub>5</sub> B <sub>15</sub>	7.26
11	Fe <sub>80</sub> Si <sub>12</sub> B <sub>8</sub>	7.26

reported in Table 2, was calculated by substituting the critical diameter ( $d_c$ ) into Eq. (A.1):

$$R_C \approx \left| \frac{12}{\rho \cdot C_p} \cdot (T_d - T_f) \frac{k_g}{d_c^2} \right| \quad (\text{A.3})$$

The numerical values used in this calculation were  $C_p = 35$  J/(mol·K) [59],  $T_d = 300$  K,  $T_f = 1973$  K,  $k_g = 0.150$  W/(m·K) for He [57] and the density of the alloys ( $\rho$ ) measured by He pycnometry (see Table A1).

## References

- [1] P. Duwez, R.H. Willens, W. Klement, Continuous series of metastable solid solutions in silver-copper alloys, *J. Appl. Phys.* 31 (1960) 1136–1137, <https://doi.org/10.1063/1.1735777>.
- [2] H.X. Li, Z.C. Lu, S.L. Wang, Y. Wu, Z.P. Lu, Fe-based bulk metallic glasses: Glass formation, fabrication, properties and applications, *Prog. Mater. Sci.* 103 (2019) 235–318, <https://doi.org/10.1016/j.pmatsci.2019.01.003>.
- [3] C.A. Queiroz, J. Sesták, Aspects of the non-crystalline state, *Phys. Chem. Glas. Eur. J. Og Glas. Sci. Technol. Part B.* 51 (2010) 165–172.
- [4] P.K. Gupta, Non-crystalline solids: glasses and amorphous solids, *J. Non. Cryst. Solids.* 195 (1996) 158–164, [https://doi.org/10.1016/0022-3093\(95\)00502-1](https://doi.org/10.1016/0022-3093(95)00502-1).
- [5] I.-R. Lu, G. Wilde, G.P. Görlner, R. Willnecker, Thermodynamic properties of Pd-based glass-forming alloys, *J. Non. Cryst. Solids.* 250–252 (1999) 577–581, [https://doi.org/10.1016/S0022-3093\(99\)00135-0](https://doi.org/10.1016/S0022-3093(99)00135-0).
- [6] Z. Mahbooba, L. Thorsson, M. Onoson, P. Skoglund, H. West, T. Horn, C. Rock, E. Vogli, O. Harrysson, Additive manufacturing of an iron-based bulk metallic glass larger than the critical casting thickness, *Appl. Mater. Today.* 11 (2018) 264–269, <https://doi.org/10.1016/j.apmt.2018.02.011>.
- [7] A. Masood, V. Ström, L. Belova, K.V. Rao, J. Ågren, Effect of Ni-substitution on glass forming ability, mechanical, and magnetic properties of FeNbY bulk metallic glasses, *J. Appl. Phys.* 113 (2013), 013505, <https://doi.org/10.1063/1.4772753>.
- [8] A. Masood, L. Belova, V. Ström, On the correlation between glass forming ability (GFA) and soft magnetism of Ni-substituted Fe-based metallic glassy alloys, *J. Magn. Magn. Mater.* 504 (2020), 166667, <https://doi.org/10.1016/j.jmmm.2020.166667>.
- [9] E. Dastanpour, M.H. Enayati, A. Masood, V. Ström, On the glass forming ability (GFA), crystallization behavior and soft magnetic properties of nanomet-substituted alloys, *J. Non. Cryst. Solids.* 529 (2020), 119774, <https://doi.org/10.1016/j.jnoncrysol.2019.119774>.
- [10] D. Turnbull, Under what conditions can a glass be formed? *Contemp. Phys.* 10 (1969) 473–488, <https://doi.org/10.1080/00107516908204405>.
- [11] Z.P. Lu, Y. Li, S.C. Ng, Reduced glass transition temperature and glass forming ability of bulk glass forming alloys, *J. Non. Cryst. Solids.* 270 (2000) 103–114, [https://doi.org/10.1016/S0022-3093\(00\)00064-8](https://doi.org/10.1016/S0022-3093(00)00064-8).
- [12] I.W. Donald, H.A. Davies, Prediction of glass-forming ability for metallic systems, *J. Non. Cryst. Solids.* 30 (1978) 77–85, [https://doi.org/10.1016/0022-3093\(78\)90058-3](https://doi.org/10.1016/0022-3093(78)90058-3).
- [13] A. Takeuchi, A. Inoue, Classification of bulk metallic glasses by atomic size difference, heat of mixing and period of constituent elements and its application to characterization of the main alloying element, *Mater. Trans.* 46 (2005) 2817–2829, <https://doi.org/10.2320/matertrans.46.2817>.
- [14] C. Suryanarayana, A. Inoue, *Bulk Metallic Glasses*, CRC/Taylor & Francis, US, 2011.
- [15] A. Inoue, T. Zhang, T. Masumoto, Glass-forming ability of alloys, *J. Non. Cryst. Solids.* 156–158 (1993) 473–480, [https://doi.org/10.1016/0022-3093\(93\)90003-G](https://doi.org/10.1016/0022-3093(93)90003-G).
- [16] M. Saad, M. Poulain, Glass forming ability criterion, *Mater. Sci. Forum.* 19–20 (1987) 11–18, <https://doi.org/10.4028/www.scientific.net/msf.19-20.11>.
- [17] Z.P. Lu, C.T. Liu, A new glass-forming ability criterion for bulk metallic glasses, *Acta Mater.* 50 (2002) 3501–3512, [https://doi.org/10.1016/S1359-6454\(02\)00166-0](https://doi.org/10.1016/S1359-6454(02)00166-0).
- [18] Q. Chen, J. Shen, D. Zhang, H. Fan, J. Sun, D.G. McCartney, A new criterion for evaluating the glass-forming ability of bulk metallic glasses, *Mater. Sci. Eng. A.* 433 (2006) 155–160, <https://doi.org/10.1016/j.msea.2006.06.053>.
- [19] G.J. Fan, H. Choo, P.K. Liaw, A new criterion for the glass-forming ability of liquids, *J. Non. Cryst. Solids.* 353 (2007) 102–107, <https://doi.org/10.1016/j.jnoncrysol.2006.08.049>.
- [20] X.H. Du, J.C. Huang, C.T. Liu, Z.P. Lu, New criterion of glass forming ability for bulk metallic glasses, *J. Appl. Phys.* 101 (2007) 23–25, <https://doi.org/10.1063/1.2718286>.
- [21] Z. Long, H. Wei, Y. Ding, P. Zhang, G. Xie, A. Inoue, A new criterion for predicting the glass-forming ability of bulk metallic glasses, *J. Alloys Compd.* 475 (2009) 207–219, <https://doi.org/10.1016/j.jallcom.2008.07.087>.
- [22] Z.Z. Yuan, S.L. Bao, Y. Lu, D.P. Zhang, L. Yao, A new criterion for evaluating the glass-forming ability of bulk glass forming alloys, *J. Alloys Compd.* 459 (2008) 251–260, <https://doi.org/10.1016/j.jallcom.2007.05.037>.
- [23] E.S. Park, W.T. Kim, D.H. Kim, A simple model for determining alloy composition with large glass forming ability in ternary alloys, *Metall. Mater. Trans. A Phys. Metall. Mater. Sci.* 32 (2001) 200–202, <https://doi.org/10.1007/s11661-998-0334-4>.
- [24] E.S. Park, D.H. Kim, W.T. Kim, Parameter for glass forming ability of ternary alloy systems, *Appl. Phys. Lett.* 86 (2005), 061907, <https://doi.org/10.1063/1.1862790>.
- [25] T. Egami, Y. Waseda, Atomic size effect on the glass forming ability of metallic alloys, *J. Non. Cryst. Solids.* 64 (1984) 113–134.
- [26] K. Mondal, B.S. Murty, On the parameters to assess the glass forming ability of liquids, *J. Non. Cryst. Solids.* 351 (2005) 1366–1371, <https://doi.org/10.1016/j.jnoncrysol.2005.03.006>.
- [27] J.J. Han, C.P. Wang, J. Wang, X.J. Liu, Y. Wang, Z.K. Liu, Compositional design of Fe-based multi-component bulk metallic glass based on CALPHAD method, *Mater. Des.* 126 (2017) 47–56, <https://doi.org/10.1016/j.matdes.2017.04.030>.
- [28] L. Shi, K. Yao, Composition design for Fe-based soft magnetic amorphous and nanocrystalline alloys with high Fe content, *Mater. Des.* 189 (2020), 108511, <https://doi.org/10.1016/j.matdes.2020.108511>.
- [29] K. Ackland, A. Masood, S. Kulkarni, P. Stamenov, Ultra-soft magnetic Co-Fe-Si-Nb amorphous alloys for high frequency power applications, *AIP Adv* 8 (2018), <https://doi.org/10.1063/1.5007707>.
- [30] H. Ahmadian, A. Masood, Z. Pavlovic, K.L. Alvarez, C. Ómáthúna, P. McCloskey, P. Stamenov, On the mechanisms limiting power loss in amorphous CoFeB-based melt-spun ribbons, *J. Magn. Magn. Mater.* 502 (2020), 166535, <https://doi.org/10.1016/j.jmmm.2020.166535>.
- [31] A. Masood, H.A. Baghbaderani, K.L. Alvarez, J.M. Blanco, Z. Pavlovic, V. Ström, P. Stamenov, C.O. Mathuna, P. McCloskey, High-frequency power loss mechanisms in ultra-thin amorphous ribbons, *J. Magn. Magn. Mater.* 519 (2021), 167469, <https://doi.org/10.1016/j.jmmm.2020.167469>.
- [32] M. Hagiwara, A. Inoue, T. Masumoto, Mechanical properties of Fe-Si-B amorphous wires produced by in-rotating-water spinning method, *Metall. Trans. A.* 13 (1982) 373–382, <https://doi.org/10.1007/BF02643346>.
- [33] G. Herzer, Modern soft magnets: Amorphous and nanocrystalline materials, *Acta Mater.* 61 (2013) 718–734, <https://doi.org/10.1016/j.actamat.2012.10.040>.
- [34] R.M. German, *Powder Metallurgy and Particulate Materials Processing*, Metal Powder Industries Federation (MPIF), Princeton, NJ, USA, 2005.
- [35] K.L. Alvarez, H.A. Baghbaderani, J.M. Martín, N. Burgos, M. Ipatov, Z. Pavlovic, P. McCloskey, A. Masood, J. Gonzalez, Novel Fe-based amorphous and nanocrystalline powder cores for high-frequency power conversion, *J. Magn. Magn. Mater.* 501 (2020), 166457, <https://doi.org/10.1016/j.jmmm.2020.166457>.
- [36] Z. Guo, J. Wang, W. Chen, D. Chen, H. Sun, Z. Xue, C. Wang, Crystal-like microstructural Finemet/FeSi compound powder core with excellent soft magnetic properties and its loss separation analysis, *Mater. Des.* 192 (2020), 108769, <https://doi.org/10.1016/j.matdes.2020.108769>.

- [37] A.J. Yule, J.J. Dunkley, *Atomization of Melts for Powder Production and Spray Deposition*, Oxford University Press, UK Oxford, 1994.
- [38] T. Sato, Study on powder properties of Fe-P-C and Fe-B-Si alloy powders prepared by water atomization, *J. Mater. Sci.* 26 (1991) 2329–2336, <https://doi.org/10.1007/BF01130177>.
- [39] M. Hagiwara, A. Inoue, T. Masumoto, The critical thickness for the formation of Fe-, Ni- and Co-based amorphous alloys with metalloids, *Sci. Reports Res. Institutes Tohoku Univ. Ser. a-Physics Chem. Metall.* 29 (1981) 351–358.
- [40] F.E. Luborsky, I. Reeve, H.A. Davies, H.H. Liebermann, Effect of Fe-B-Si composition on maximum thickness for casting amorphous metals, *IEEE Trans. Magn.* 18 (1982) 1385–1387, <https://doi.org/10.1109/TMAG.1982.1062025>.
- [41] M. Schütte, R. Wartchow, M. Binnewies, Shape controlling synthesis - Formation of Fe<sub>3</sub>Si by the reaction of iron with silicon tetrachloride and crystal structure refinement, *Zeitschrift Fur Anorg. Und Allg. Chemie.* 629 (2003) 1846–1850, <https://doi.org/10.1002/zaac.200300125>.
- [42] M. Polcarová, K. Godwod, J. Bák-Misiuk, S. Kadečková, J. Brádl, Lattice parameters of Fe-Si alloy single crystals, *Phys. Status Solidi.* 106 (1988) 17–23, <https://doi.org/10.1002/pssa.2211060103>.
- [43] K.L. Alvarez, J.M. Martín, M. Ipatov, L. Dominguez, J. Gonzalez, Magnetic properties of annealed amorphous Fe<sub>72.5</sub>Si<sub>12.5</sub>B<sub>15</sub> alloy obtained by gas atomization technique, *IEEE Trans. Magn.* 54 (2018), 2002405, <https://doi.org/10.1109/TMAG.2018.2839258>.
- [44] K.L. Alvarez, J.M. Martín, M. Ipatov, L. Dominguez, J. Gonzalez, Effect of Composition and Particle Size on the Soft Magnetic Character of Fe-Rich Amorphous Alloys Obtained by Gas Atomization. Euro PM2019, European Powder Metallurgy Association (EPMA), Maastricht, The Netherlands, 2019, pp. 1–6.
- [45] A. Zaluska, H. Matyja, Crystallization characteristics of amorphous Fe-Si-B alloys, *J. Mater. Sci.* 18 (1983) 2163–2172, <https://doi.org/10.1007/BF00555011>.
- [46] K.L. Alvarez, J.M. Martín, M. Ipatov, J. Gonzalez, Soft magnetic amorphous alloys (Fe-rich) obtained by gas atomisation technique, *J. Alloys Compd.* 735 (2018) 2646–2652, <https://doi.org/10.1016/j.jallcom.2017.11.272>.
- [47] Burton, *Amorphous Metallic Alloys*, 1st ed., Butterworths, UK, 1983.
- [48] M.E. Brown, *Introduction to thermal analysis: techniques and applications*, 2001. <https://doi.org/10.1017/CBO9781107415324.004>.
- [49] M. Hagiwara, A. Inoue, T. Masumoto, Production of amorphous CoSiB and CoMSiB (M = Group IV - VIII transition metals) wires by a method employing melt spinning into rotating water and some properties of the wires, *Mater. Sci. Eng.* 54 (1982) 197–207, [https://doi.org/10.1016/0025-5416\(82\)90114-8](https://doi.org/10.1016/0025-5416(82)90114-8).
- [50] U. Carow-Watamura, D.V. Louzguine, A. Takeuchi, B-Fe-Si (144), in: Y. Kawazoe, U. Carow-Watamura, J.Z. Yu (Eds.), *Phys. Prop. Ternary Amorph. Alloy. Part 2 Syst. from B-Be-Fe to Co-W-Zr*. Landolt-Börnstein - Gr. III Condens. Matter (Numerical Data Funct. Relationships Sci. Technol., Springer, Berlin, Heidelberg, 2011, pp. 200–253, [https://doi.org/10.1007/978-3-642-13850-8\\_44](https://doi.org/10.1007/978-3-642-13850-8_44).
- [51] A. Takeuchi, A. Inoue, Calculations of mixing enthalpy and mismatch entropy for ternary amorphous alloys, *Mater. Trans. JIM.* 41 (2000) 1372–1378, <https://doi.org/10.2320/matertrans1989.41.1372>.
- [52] Z.J. Yan, J.F. Li, S.R. He, Y.H. Zhou, Evaluation of the optimum solute concentration for good glass forming ability in multicomponent metallic glasses, *Mater. Res. Bull.* 38 (2003) 681–689, [https://doi.org/10.1016/S0025-5408\(03\)00010-2](https://doi.org/10.1016/S0025-5408(03)00010-2).
- [53] A. Tabeshian, H. Mao, L. Arnberg, R.E. Aune, Investigation of glass forming ability in the Zr-rich part of the Zr-Fe-Al ternary system, *J. Appl. Phys.* 125 (2019), 065101, <https://doi.org/10.1063/1.5066554>.
- [54] D.D.E. Brennhaugen, H. Mao, D.V. Louzguine-Luzgin, L. Arnberg, R.E. Aune, Predictive modeling of glass forming ability in the Fe-Nb-B system using the CALPHAD approach, *J. Alloys Compd.* 707 (2017) 120–125, <https://doi.org/10.1016/j.jallcom.2016.12.049>.
- [55] H.A. Baghbaderani, A. Masood, K.L. Alvarez, C.Ó. Mathúna, P. McCloskey, P. Stamenov, CALPHAD-assisted development of in-situ nanocrystallised melt-spun Co-Fe-B alloy with high Bs (1.57T), *J. Alloys Compd.* 877 (2021), 160194, <https://doi.org/10.1016/j.jallcom.2021.160194>.
- [56] H. Shiwen, L. Yong, G. Sheng, Cooling rate calculation of non-equilibrium aluminum alloy powders prepared by gas atomization, *Rare Met. Mater. Eng.* 38 (2009) 353–356.
- [57] A. Inoue, Light-metal based amorphous alloys. *Curr. Top. Amorph. Mater.*, Elsevier B.V., 1993, pp. 159–166, <https://doi.org/10.1016/B978-0-444-81576-7.50023-X>.
- [58] N. Ciftci, N. Ellendt, R. Von Barga, H. Henein, L. Mädler, V. Uhlenwinkel, Atomization and characterization of a glass forming alloy {(Fe<sub>0.6</sub>Co<sub>0.4</sub>)<sub>0.75</sub>B<sub>0.2</sub>Si<sub>0.05</sub>}<sub>96</sub>Nb<sub>4</sub>, *J. Non. Cryst. Solids.* 394–395 (2014) 36–42, <https://doi.org/10.1016/j.jnoncrysol.2014.03.023>.
- [59] J. Zhang, H. Fujimori, A. Inoue, T. Masumoto, Specific heat behaviour on soft magnetic thick amorphous ribbons of an Fe-B-Si alloy, *Mater. Sci. Eng.* 99 (1988) 35–38, [https://doi.org/10.1016/0025-5416\(88\)90286-8](https://doi.org/10.1016/0025-5416(88)90286-8).